



## UvA-DARE (Digital Academic Repository)

### Search for Coherent Elastic Scattering of Solar $^8\text{B}$ Neutrinos in the XENON1T Dark Matter Experiment

Aprile, E.; Angevaare, J.R.; Bruenner, S. ; Colijn, A.P.; Decowski, M.P.; Gaemers, P. ; XENON Collaboration

**DOI**

[10.1103/PhysRevLett.126.091301](https://doi.org/10.1103/PhysRevLett.126.091301)

**Publication date**

2021

**Document Version**

Other version

**Published in**

Physical Review Letters

**License**

CC BY

[Link to publication](#)

**Citation for published version (APA):**

Aprile, E., Angevaare, J. R., Bruenner, S., Colijn, A. P., Decowski, M. P., Gaemers, P., & XENON Collaboration (2021). Search for Coherent Elastic Scattering of Solar  $^8\text{B}$  Neutrinos in the XENON1T Dark Matter Experiment. *Physical Review Letters*, 126(9), Article 091301. <https://doi.org/10.1103/PhysRevLett.126.091301>

**General rights**

It is not permitted to download or to forward/distribute the text or part of it without the consent of the author(s) and/or copyright holder(s), other than for strictly personal, individual use, unless the work is under an open content license (like Creative Commons).

**Disclaimer/Complaints regulations**

If you believe that digital publication of certain material infringes any of your rights or (privacy) interests, please let the Library know, stating your reasons. In case of a legitimate complaint, the Library will make the material inaccessible and/or remove it from the website. Please Ask the Library: <https://uba.uva.nl/en/contact>, or a letter to: Library of the University of Amsterdam, Secretariat, Singel 425, 1012 WP Amsterdam, The Netherlands. You will be contacted as soon as possible.

*UvA-DARE is a service provided by the library of the University of Amsterdam (<https://dare.uva.nl>)*

## SUPPLEMENTAL MATERIAL

### Waveform Simulation

The S1 and S2 detection efficiencies in the CE $\nu$ NS ROI cannot easily be measured with a calibration source. Therefore, we use a waveform simulation, which produces PMT waveforms in the CE $\nu$ NS ROI, to calculate those efficiencies.

Some of the S1s detected by two or more PMTs do not meet the requirement that hits on those PMTs occur within 50 ns. The fraction of the S1s passing this tight-coincidence requirement thus correlates with the S1 width. We use an exponential function to describe the distribution of photons detected by PMTs in the simulation to facilitate tuning of the S1 width. The S1 time distribution is independent of the number of hits in XENON1T data. This allows us to calibrate the exponential function by matching simulated S1s to those in data.

Four more detector effects are included in the simulation: the probability that the PMT photocathode emits two photoelectrons when absorbing one photon, the electronic noise level, the single photoelectron spectrum of the PMTs, and PMT after-pulses. The full simulation process establishes the relation between the number of detected photons and the size of the S1 and S2 [1].

The mean and spread of the S1 width distribution vary with the size of the S1. Simulated waveforms and XENON1T data are processed with the same software. The S1 width parameter in the simulation is tuned to minimize the chi-square between simulated and observed mean width as shown in Fig. 5.

The software trigger efficiency of the S2 varies with its size and the position of the event. Events from the deeper part of the detector produce wider S2s, and have a lower trigger efficiency. Specifically, in waveform simulation, we use effective models to reproduce the diffusion, size, and temporal distribution of ionization signals. Together with the four detector effects mentioned above, the simulation output is compared to background S2s originating on the detector wall in both width and triggered fraction, since wall events have a smaller S2 size due to charge loss on surfaces. The excellent matching between simulated and wall events, shown in Fig. 5 and Fig. 6, validates the response of the detector to small S2s.

### Signal expectation

From the standard solar model, the energy of solar  $^8\text{B}$  neutrinos is below  $\sim 20$  MeV, giving a maximum momentum transfer  $q_{\text{max}} \sim 40$  MeV, much smaller than the Z boson mass [2]. Under this condition, the Standard Model predicts that the tree-level differential CE $\nu$ NS

cross section is given by:

$$\frac{d\sigma_{\text{CE}\nu\text{NS}}}{dE_r} = \frac{G_F^2}{4\pi} Q_w^2 M \left(1 - \frac{ME_r}{2E_\nu^2}\right) F(E_r)^2, \quad (1)$$

where  $E_r$  is the NR energy,  $G_F$  is the Fermi constant,  $M$  is the target nuclear mass of the recoiling atom,  $E_\nu$  is the incoming neutrino energy,  $F(E_r)$  is the nuclear form factor, and  $Q_w$  is the nuclear weak charge [3]. Here, we have neglected the contribution from the hadronic axial-vector current, because the spin-dependent structure factors are negligible compared with spin-independent structure factors for xenon [4]. Since  $M \gg E_\nu \gg E_r$ , terms of higher order in  $E_r/E_\nu$  are dropped as well.

We also consider a non-standard interaction following [5, 6], where the weak charge in electron neutrino scattering is replaced by  $Q_w \rightarrow \tilde{Q}_w = N(1 + 2\varepsilon_{ee}^{uV} + 4\varepsilon_{ee}^{dV}) + Z(4\sin^2\theta_w - 1 + 4\varepsilon_{ee}^{uV} + 2\varepsilon_{ee}^{dV})$ , with two non-standard couplings  $\varepsilon_{ee}^{uV}$  and  $\varepsilon_{ee}^{dV}$ . Neutrino oscillation must be included, since our model assumes that only electron neutrinos have non-zero non-standard interactions. In the energy range of solar  $^8\text{B}$  neutrinos, their oscillation to other flavors through interactions with matter in the Sun (the MSW effect) is important [7]. In the standard model, this effect can be interpreted as an equivalent index of refraction  $n = 1 + \sqrt{2}G_F N_e/E_\nu$  for electron neutrinos, with  $N_e$  being the electron number density. Our model assumes two additional non-standard interactions  $\varepsilon_{ee}^{uV}$  and  $\varepsilon_{ee}^{dV}$ , so the index of refraction should be modified to be  $\tilde{n} = 1 + \sqrt{2}G_F(N_e + \varepsilon_{ee}^{uV} N_u + \varepsilon_{ee}^{dV} N_d)/E_\nu$ , where  $N_u$  ( $N_d$ ) is the number density of up (down) quarks. Thus, the inclusion of non-standard interactions also makes the survival probability of electron neutrinos  $P_e$  epsilon-dependent [8]. The neutrino oscillation parameters in the following calculation are from [9]. Using  $\Phi = (5.25 \pm 0.20) \times 10^6 \text{ cm}^{-2}\text{s}^{-1}$  and letting  $\eta(E_r)$  be the NR acceptance, the final expected CE $\nu$ NS rate from solar  $^8\text{B}$  neutrinos is

$$R(\varepsilon_{ee}^{uV}, \varepsilon_{ee}^{dV}) = \frac{1}{M} \int \frac{d\sigma}{dE_r} \frac{d\Phi}{dE_\nu} \eta(E_r) dE_\nu dE_r, \quad (2)$$

where  $d\sigma/dE_r$  is given by

$$\frac{d\sigma}{dE_r} = \frac{d\sigma_{\text{CE}\nu\text{NS}}}{dE_r} \frac{\tilde{Q}_w^2}{Q_w^2} P_e + \frac{d\sigma_{\text{CE}\nu\text{NS}}}{dE_r} (1 - P_e). \quad (3)$$

So the upper limit on  $\Phi$  can be converted into  $\varepsilon_{ee}^{uV}$ - $\varepsilon_{ee}^{dV}$  space by solving:

$$\langle R(\varepsilon_{ee}^{uV}, \varepsilon_{ee}^{dV}) \rangle < \frac{\Phi_{\text{limit}}}{\Phi} \langle R(\varepsilon_{ee}^{uV} = 0, \varepsilon_{ee}^{dV} = 0) \rangle, \quad (4)$$

where  $\langle \cdot \rangle$  denotes the isotopic average (assuming natural abundances in xenon), and  $\Phi_{\text{limit}} = 1.4 \times 10^7 \text{ cm}^{-2}\text{s}^{-1}$  is the upper limit on  $\Phi$  (see Results section).

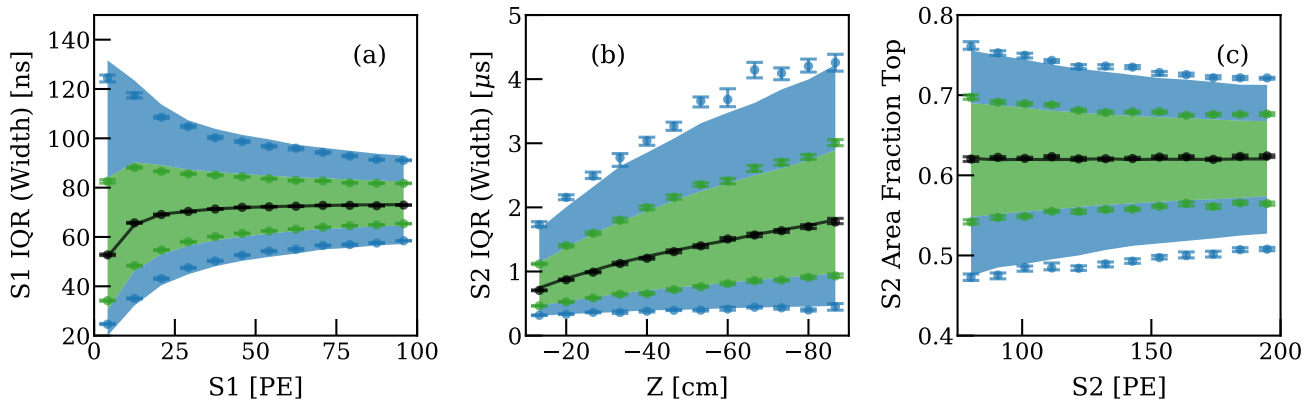


FIG. 5. Matching of the S1 and S2 properties of the waveform simulation and detector data originating from the TPC wall. The plots show (a) the interquartile range (IQR), the range of time covering the central 50% area, as a function of S1 size, (b) IQR of S2 < 200 PE as a function of depth ( $Z$ ), and (c) the fraction of signal detected by the top PMT array in each S2 ( $-10 \text{ cm} < Z < 90 \text{ cm}$ ). The dots denote quantiles of the detector data, corresponding to  $\pm 2\sigma$  (blue),  $\pm 1\sigma$  (green), and median (black). Colored bands show the same quantiles with the simulation data. Both detector and simulation data are events close to the wall, with the same position, S1 size, and S2 size distributions.

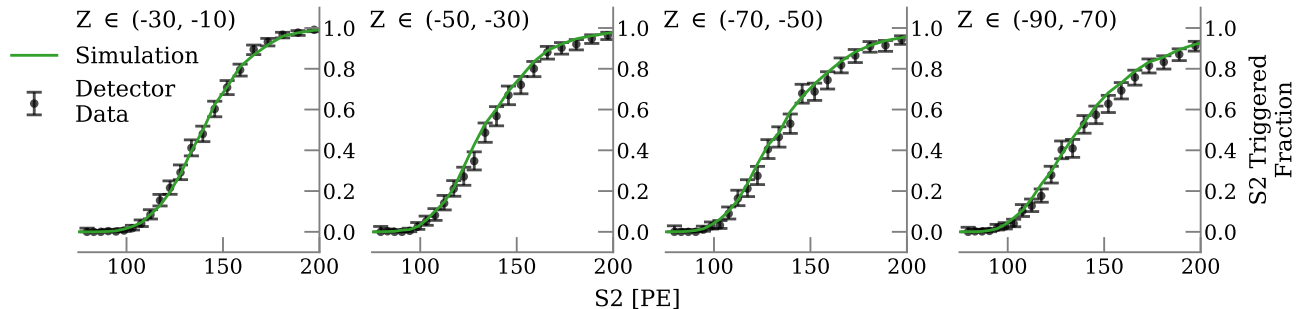


FIG. 6. Efficiencies (fraction of S2 passed) of the software trigger as a function of the S2 size at different depth ( $Z$ ) ranges (in cm) show agreement between the simulation and detector data. The black dots correspond to the events in detector data, that were triggered by their S1. The green line shows the fraction of simulated S2 passing the trigger, produced with the same position distribution as the S1-triggered detector data.

### More details on the AC background

The rates of isolated S1s and isolated S2s are significantly increased following high-energy events, mainly due to gamma-ray backgrounds. In XENON1T, we found that the rate of single-electron S2s and lone hits on PMTs are correlated with  $S2_{\text{prev}}/\Delta t_{\text{prev}}$ . Fig. 7 shows the distribution of  $S2_{\text{prev}}/\Delta t_{\text{prev}}$  for both isolated S1s and high-energy events themselves. The distribution for high-energy events reflects that of signal events, since neither are correlated with preceding S2s. Thus, a selection requiring  $S2_{\text{prev}}/\Delta t_{\text{prev}} \leq 12 \text{ PE}/\mu\text{s}$  rejects 65% of isolated S1s (and consequently AC events) with 87% signal acceptance.

Although the selection on  $S2_{\text{prev}}/\Delta t_{\text{prev}}$  also suppresses the rate of isolated S2s, those that remain near the 80 PE threshold are still correlated with  $S2_{\text{prev}}/\Delta t_{\text{prev}}$ . To remove this correlation, we utilize the horizontal ( $X, Y$ ) positions of isolated S2s, calcu-

lated from fitting their PMT distribution patterns, similar to [10]. We investigate the horizontal spatial distance of isolated S2s from previous high energy events,  $\sqrt{(X - X_{\text{prev}})^2 + (Y - Y_{\text{prev}})^2}$ , to quantify the correlation between them, as shown in Fig. 8. A distinctive population with small  $\sqrt{(X - X_{\text{prev}})^2 + (Y - Y_{\text{prev}})^2}$  values is seen near the 80 PE threshold. A cut, shown as a red line, rejects > 99% of events that occur at the same ( $X, Y$ ) position as the preceding event but are reconstructed with non-zero mean-squared distance due to uncertainties in the reconstructed positions. The acceptance of this cut as a function of S2 is studied by randomly associating two uncorrelated events, and ranges from 92% at 120 PE to > 99% for S2 > 500 PE.

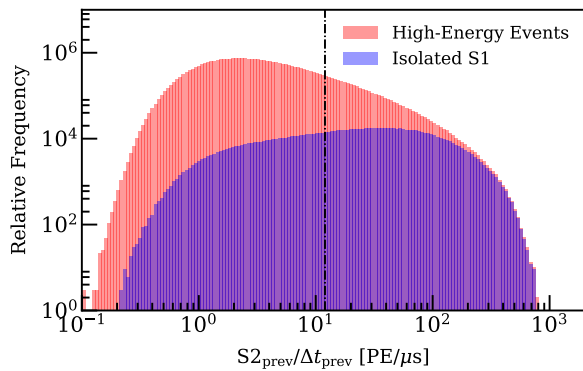


FIG. 7. Distribution in  $S2_{\text{prev}}/\Delta t_{\text{prev}}$  space of both high-energy events and isolated S1s immediately preceding them. At large  $S2_{\text{prev}}/\Delta t_{\text{prev}}$  values, a significant fraction of high energy events contain an isolated S1 before the trigger. The discrimination between signal events (which have the same distribution as high-energy events) and isolated S1s allows the selection  $S2_{\text{prev}}/\Delta t_{\text{prev}} \leq 12 \text{ PE}/\mu\text{s}$ , shown as a vertical black dash-dotted line, which rejects 65% of background with 87% signal acceptance.

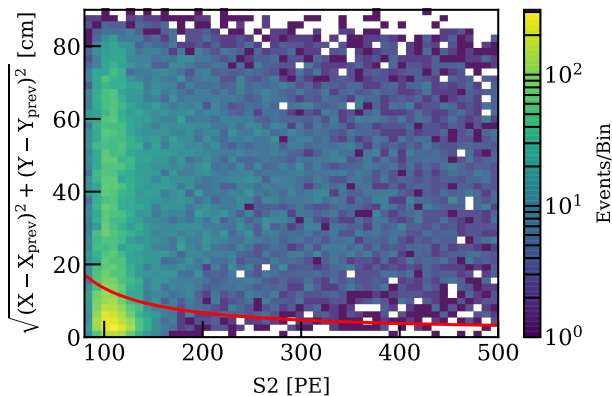


FIG. 8. Horizontal spatial distance of isolated S2s with respect to previous high-energy events. Events below the red line are removed to ensure no correlation between isolated S2s and the preceding high-energy event.

### Details on constructing confidence volumes

Since the NR response uncertainty is large, the test statistic distribution for confidence intervals will depend on the true values of  $\Phi$ ,  $Q_y$ , and  $L_y$ . To compute a unified confidence interval in all these parameters in the manner of [1] and the DM results in this paper, we would have to estimate the distribution of the test statistic using toy-MC computations in these three dimensions. However, the strong degeneracy between these parameters allows us to avoid this extensive computation. For the relevant range for this search, and the low number of events expected, the  $\text{CE}\nu\text{NS}$  model shape changes so

little with  $Q_y$  and  $L_y$  that inference results are not affected: Computing the discovery significance of toy-MC simulations either fitting these shape parameters, fixing them to their true values or shifting them by  $+2\sigma$  each yielded no discernible bias, and a spread compatible with toy-MC variation only. Therefore, only when computing confidence intervals on  $\Phi^1$ ,  $Q_y$ , and  $L_y$ , the  $\text{CE}\nu\text{NS}$  model shape is fixed, and these variables appear in the likelihood only via the expression for the expectation value of detected  $\text{CE}\nu\text{NS}$  events,  $\mu_{\text{CE}\nu\text{NS}}(\Phi, Q_y, L_y)$ . Therefore, we can compute the profile likelihood ratio and toy-MC estimates of the test statistic distribution in the space of  $\mu_{\text{CE}\nu\text{NS}}$  alone. External constraints on  $\Phi$ ,  $L_y$ , and  $Q_y$  are implemented as terms  $\lambda_F$ ,  $\lambda_{L_y}$ , and  $\lambda_{Q_y}$ , corresponding to the profiled log-likelihood-ratios for Gaussian measurements of each parameter. We combine the XENON1T profiled log-likelihood ratio  $\lambda_{\text{Xe1T}}(\mu_{\text{CE}\nu\text{NS}}(\Phi, Q_y, L_y))$  and different combinations of external constraints into test statistics  $\Lambda$ :

$$\begin{aligned} \Lambda_A(\Phi, Q_y, L_y) &= \lambda_{\text{Xe1T}}(\mu_{\text{CE}\nu\text{NS}}(\Phi, Q_y, L_y)) \\ \Lambda_B(\Phi, Q_y, L_y) &= \lambda_{\text{Xe1T}}(\mu_{\text{CE}\nu\text{NS}}(\Phi, Q_y, L_y)) + \\ &\quad \lambda_{Q_y}(Q_y) + \lambda_{\text{CE}\nu\text{NS}}(\Phi) \\ \Lambda_C(\Phi, Q_y, L_y) &= \lambda_{\text{Xe1T}}(\mu_{\text{CE}\nu\text{NS}}(\Phi, Q_y, L_y)) + \\ &\quad \lambda_{Q_y}(Q_y) + \lambda_{L_y}(L_y). \end{aligned} \quad (5)$$

For each  $\Lambda$ , the toy-MC results of  $\lambda_{\text{Xe1T}}(\mu_{\text{CE}\nu\text{NS}})$  is combined with random realizations of the other profiled likelihoods in a grid of  $\Phi$ ,  $Q_y$ , and  $L_y$  to provide the 90th percentile of  $\Lambda$  for each point in parameter space, which is compared with  $\Lambda(\Phi, Q_y, L_y)$  to construct confidence intervals. The test statistic  $\Lambda_A$ , shown in green in Fig. 3 in the main text, represents the confidence interval using the XENON1T data only. The strong anti-correlation between  $\Phi$  and  $L_y$  is apparent in Fig. 3 (top). To compute a confidence interval on  $L_y$ , we include constraints on  $Q_y$  [11] and  $\Phi$  [12] in  $\Lambda_B$ , shown in dark blue in Fig. 3 in the main text. Last, combining XENON1T, and constraints on  $Q_y$  [11] and  $L_y$  [13, 14] into  $\Lambda_C$  yields an upper limit on the  $\text{CE}\nu\text{NS}$  interaction rate  $\Phi$ .

- 
- [1] E. Aprile *et al.* (XENON Collaboration), XENON1T dark matter data analysis: Signal and background models and statistical inference, *Phys. Rev. D* **99**, 112009 (2019), arXiv:1902.11297 [physics.ins-det].
  - [2] J. Billard, L. Strigari, and E. Figueroa-Feliciano, Implication of neutrino backgrounds on the reach of next generation dark matter direct detection experiments, *Phys. Rev. D* **89**, 023524 (2014), arXiv:1307.5458 [hep-ph].

<sup>1</sup> Also used for the non-standard neutrino interaction result

- [3] D. Z. Freedman, Coherent effects of a weak neutral current, *Phys. Rev. D* **9**, 1389 (1974).
- [4] E. Aprile *et al.* (XENON Collaboration), Constraining the spin-dependent WIMP-nucleon cross sections with XENON1T, *Phys. Rev. Lett.* **122**, 141301 (2019), [arXiv:1902.03234](#).
- [5] D. Akimov *et al.* (COHERENT Collaboration), First Detection of Coherent Elastic Neutrino-Nucleus Scattering on Argon, [arXiv:2003.10630 \[nucl-ex\]](#) (2020).
- [6] S. Brice *et al.*, A method for measuring coherent elastic neutrino-nucleus scattering at a far off-axis high-energy neutrino beam target, *Phys. Rev. D* **89**, 072004 (2014), [arXiv:1311.5958 \[physics.ins-det\]](#).
- [7] L. Wolfenstein, Neutrino Oscillations in Matter, *Phys. Rev. D* **17**, 2369 (1978).
- [8] A. Friedland, C. Lunardini, and C. Pena-Garay, Solar neutrinos as probes of neutrino matter interactions, *Phys. Lett. B* **594**, 347 (2004), [arXiv:hep-ph/0402266](#).
- [9] F. Capozzi, E. Di Valentino, E. Lisi, A. Marrone, A. Melchiorri, and A. Palazzo, Global constraints on absolute neutrino masses and their ordering, *Phys. Rev. D* **95**, 096014 (2017), [Addendum: *Phys.Rev.D* 101, 116013 (2020)], [arXiv:2003.08511 \[hep-ph\]](#).
- [10] E. Aprile *et al.* (XENON Collaboration), XENON1T Dark Matter Data Analysis: Signal Reconstruction, Calibration and Event Selection, *Phys. Rev. D* **100**, 052014 (2019), [arXiv:1906.04717 \[physics.ins-det\]](#).
- [11] B. Lenardo *et al.*, Low-Energy Physics Reach of Xenon Detectors for Nuclear-Recoil-Based Dark Matter and Neutrino Experiments, *Phys. Rev. Lett.* **123**, 231106 (2019), [arXiv:1908.00518](#).
- [12] B. Aharmim *et al.* (SNO Collaboration), Combined Analysis of all Three Phases of Solar Neutrino Data from the Sudbury Neutrino Observatory, *Phys. Rev.* **C88**, 025501 (2013), [arXiv:1109.0763 \[nucl-ex\]](#).
- [13] D. S. Akerib *et al.* (LUX Collaboration), Low-energy (0.7-74 keV) nuclear recoil calibration of the LUX dark matter experiment using d-d neutron scattering kinematics (2016), [arXiv:1608.05381 \[physics.ins-det\]](#).
- [14] D. Huang, *Ultra-Low Energy Calibration of the LUX and LZ Dark Matter Detectors*, *Ph.D. thesis*, Brown U. (2020).